Journal of Computational Physics 230 (2011) 185–204

Contents lists available at ScienceDirect

Journal of Computational Physics

journal homepage: www.elsevier.com/locate/jcp

A conservative phase field method for solving incompressible two-phase flows

Pao-Hsiung Chiu *, Yan-Ting Lin

Nuclear Engineering Division, Institute of Nuclear Energy Research, Taoyuan County, Taiwan, Republic of China

ARTICLE INFO

Article history:
Received 15 April 2010
Received in revised form 4 August 2010
Accepted 15 September 2010
Available online 27 September 2010

Keywords:
Conservative phase-field method
Allen–Cahn equation
Two-phase flow
Dispersion-relation-preserving
Helmholtz smoother

ABSTRACT

In this paper a conservative phase-field method based on the work of Sun and Beckermann [Y. Sun, C. Beckermann, Sharp interface tracking using the phase-field equation, J. Comput. Phys. 220 (2007) 626–653] for solving the two- and three-dimensional two-phase incompressible Navier–Stokes equations is proposed. The present method can preserve the total mass as the Cahn–Hilliard equation, but the calculation and implementation are much simpler than that. The dispersion-relation-preserving schemes are utilized for the advection terms while the Helmholtz smoother is applied to compute the surface-tension force term. To verify the proposed method, several benchmarks are examined and shown to have good agreements with previous results. It also shows that the satisfactions of mass conservations are guaranteed.

1. Introduction

Many problems of practical importance and scientific significance involve tracking of interface between different phases, where surface tension needs to be taken into account. The necessity of capturing the time-evolving interface with a sharply varying topology and a large change in front propagation speed makes the prediction of differential equations governing the respective two-phase flow an even challenging topic.

The most common incompressible flow algorithms that have been applied to track the air/water interfaces include vortex method [1], boundary integral method [2], volume of fluid (VOF) method [3], front tracking method [4], and level set method [5,6]. The VOF method can conserve the volume exactly, but the reconstruction of the interface is a main issue. The interface reconstruction is also the problem for the front tracking method. For the level set method, interface can be implicitly defined with the zero-contour of the level set function. The main drawback of the level set method is that it cannot satisfy the volume conservation, because of re-initialization error and errors from advection calculation such as conservation error. The CLSVOF (coupled level set and volume-of-fluid) method [7], THINC (tangent of hyperbola for interface capturing) method [8,9], VOSET (volume-of-fluid and level set) method [10], and conservative level set method [11] have been proposed to resolve the problems arisen from the VOF or/and level set method. These schemes can obtain the mass-conserving and accurate solutions. However, the implementation of these schemes are still more complicated than the original VOF or level set methods.

Recently, the phase-field method [12–16] have been paid more attention on computing the two-phase flow. This method uses a phase-field to describe the phase transition. This field varies smoothly but sharply across the diffused interface region. Moreover, like the level set method, the phase-field equation can be solved over the entire computational domain without explicitly knowing the location of the interfaces. Explicitly interface tracking is then completely avoided and topology

* Corresponding author. Tel.: +886 3 4711400/6010; fax: +886 3 4711404.
E-mail address: phchiu@iner.gov.tw (P.-H. Chiu).

0021-9991/$ - see front matter © 2010 Elsevier Inc. All rights reserved.
doi:10.1016/j.jcp.2010.09.021

changes are handled naturally without any special procedures. For the phase-field method, there are two forms for the equation: Cahn–Hilliard equation [17] and Allen–Cahn equation [18]. Although Cahn–Hilliard equation can provide the mass conservation [19], spacial care must be taken when discretize the fourth-order derivative term shown in the Cahn–Hilliard equation. For the Allen–Cahn equation, only second-order derivative term is shown in the equation. However, the total mass cannot be conserved. This motivated us to find a equation that can combine both advantages of the Cahn–Hilliard and Allen–Cahn equation.

In this paper, we develop a conservative phase-field method for tracking sharp interfaces based on the work of Sun and Beckermann [15], which is motivated by the Allen–Cahn equation. Mass conservation can be obtained for the present method, and the implementation is easy. Also, the discretization errors for the present model can be expected to be lower than the ones that use the Cahn–Hilliard equation due to the fact that only second-order derivative terms are needed to be discretized.

This paper is organized as follows. Section 2 presents the derivation for the conservative phase-field method. This is followed by the presentation dispersion-relation-preserving schemes for discretizating the advection term. Section 3 presents the differential equations governing the motion of two fluids and the dispersion-relation-preserving schemes for discretizating the two-phase flow. Verification studies are presented in Section 4. Section 5 presents the simulated results to show the applicability for the proposed framework. Finally, we draw some concluding remarks in Section 6.

2. Conservative phase-field method

2.1. Phase-field equation

Assume the interface velocity is splitting into a normal interface speed and an interface velocity due to external advection. Moreover, the normal interface speed is only proportional to the interface curvature. The phase-field equation can be expressed as [15]:

$$\frac{\partial \Phi}{\partial t} + (\underline{u} \cdot \nabla)\Phi = \gamma \kappa |\nabla \Phi| \tag{1}$$

where Φ is the phase field variable, $\underline{u}$ is the velocity due to external advection, t is time and γ is a positive constant. The unit normal vector $\underline{n}$ and the curvature κ for the interface can be expressed as

$$\underline{n} = \frac{\nabla \Phi}{|\nabla \Phi|} \tag{2}$$

$$\kappa = \nabla \cdot \underline{n} = \nabla \cdot \frac{\nabla \Phi}{|\nabla \Phi|} = \frac{1}{|\nabla \Phi|}\left[\nabla^2 \Phi - \frac{\nabla \Phi \cdot \nabla |\nabla \Phi|}{|\nabla \Phi|}\right] \tag{3}$$

The Eq. (1) then can be derived as

$$\frac{\partial \Phi}{\partial t} + (\underline{u} \cdot \nabla)\Phi = \gamma\left[\nabla^2 \Phi - \frac{\nabla \Phi \cdot \nabla |\nabla \Phi|}{|\nabla \Phi|}\right] \tag{4}$$

As in [20], the following kernel function is introduced

$$\Phi = \frac{1}{2}\left[1 + \tanh\left(\frac{s}{2\epsilon}\right)\right] \tag{5}$$

where ϵ is the coefficient of the transition region which makes Φ vary between 0 to 1 with the width of $3\sqrt{2}\epsilon$, and s is the signed distance function which is the coordinate normal to the interface. Note that the above kernel function is motivated by the equilibrium profile obtained in thermodynamically derived phase-field models [20]. By choosing the above kernel function, one can get the following expressions:

$$|\nabla \Phi| = \frac{\partial \Phi}{\partial s} = \frac{\Phi(1-\Phi)}{\epsilon} \tag{6}$$

$$\frac{(\nabla \Phi \cdot \nabla)|\nabla \Phi|}{|\nabla \Phi|} = \frac{\partial^2 \Phi}{\partial s^2} = \frac{\Phi(1-\Phi)(1-2\Phi)}{\epsilon^2} \tag{7}$$

and Eq. (4) can be further derived as:

$$\frac{\partial \Phi}{\partial t} + (\underline{u} \cdot \nabla)\Phi = \gamma\left[\nabla^2 \Phi - \frac{\Phi(1-\Phi)(1-2\Phi)}{\epsilon^2}\right] \tag{8}$$

Eq. (8) have been used widely for simulating the complex interfacial pattern formation processes [20]. For the two-phase flow problem, there is no curvature-driven interface motion. One needs to eliminate this kind of motion. In this study,

the counter term approach originally introduced by Folch et al. [21] is used. In this approach, the curvature term shown in the right-hand side of Eq. (8) is subtracted back out as

$$\frac{\partial \Phi}{\partial t} + (\underline{u} \cdot \nabla)\Phi = \gamma\left[\nabla^2\Phi - \frac{\Phi(1-\Phi)(1-2\Phi)}{\epsilon^2} - |\nabla\Phi|\nabla\cdot\left(\frac{\nabla\Phi}{|\nabla\Phi|}\right)\right] \tag{9}$$

Note that the right-hand side of Eq. (9) can be derived as

$$\gamma\left[|\nabla\Phi|\nabla\cdot\left(\frac{\nabla\Phi}{|\nabla\Phi|}\right) - |\nabla\Phi|\nabla\cdot\left(\frac{\nabla\Phi}{|\nabla\Phi|}\right)\right] \tag{10}$$

and then we can cancel out the original term at the leading order [21]. From Eq. (9), we can expect that the total mass will not be conserved due to the fact that this equation is not written as a conservative form. From the analysis and numerical results in [15], the rate of convergence for the mass conservation is proportional to the mesh size if one uses the phase-field Eq. (9).

2.2. Conservative level set equation

The conservative level set method is firstly proposed by Olsson and Kreiss [11]. The following kernel function is used in their previous work:

$$\Phi = \frac{1}{1+\exp(-s/\epsilon)} \tag{11}$$

For the conservative level set method, the following two equations are needed to be solved:

$$\frac{\partial \Phi}{\partial t} + \nabla\cdot(\underline{u}\Phi) = 0 \tag{12}$$

$$\frac{\partial \Phi}{\partial \tau} + \nabla\cdot(\Phi(1-\Phi)\underline{n}) = \epsilon\nabla\cdot(\nabla\Phi) \tag{13}$$

the first equation is a advection equation for the unknown Φ, and the second equation is the compression-diffusion equation, which is proposed for the stabilization and compression of the solution to stably preserve the sharp interface. These two equation can be seen as the first step (advection) and second step (re-initialization) for the original level set method. Note that we need to solve Eq. (13) until the steady state is reached.

The conservative level set method is known to have a better mass conservation due to the fact that both steps are written as the conservative forms, as shown by Olsson and Kreiss [11]. The total mass can be exactly conserved if one uses a conservative discretization. However, it is a two-step method, and the equation for the second step is needed to be solved until steady-state is reached. Although only few time steps are sufficient in practice, the computational cost is always much larger than the one-step method such like the phase-field method (Eq. (9)). It is also worth to note that the kernel functions used for conservative level set method and phase field method are identical.

$$\frac{1}{2}\left[1+\tanh\left(\frac{s}{2\epsilon}\right)\right] = \frac{\exp(s/\epsilon)}{\exp(s/\epsilon)+1} = \frac{\frac{1}{\exp(-s/\epsilon)}}{\frac{1+\exp(-s/\epsilon)}{\exp(-s/\epsilon)}} = \frac{1}{1+\exp(-s/\epsilon)} \tag{14}$$

2.3. Derivation of the conservative phase-field equation

It have been shown by Sun and Beckermann that the phase-field equation of Eq. (9) cannot conserve the mass exactly. The rate of convergence for the mass conservation is proportional to the mesh size [15]. This will be a problem when we solving the incompressible two-phase flows. Thanks to the work of Olsson and Kreiss [11], we know that when we discrete a equation which derived as the conservative form, the total mass can be exactly conserved by conservative schemes with appropriate boundary condition (for example, no-flux boundary condition).

Motivated by the same kernel functions used for phase-field method and conservative level set method, We then derived a conservative phase-field method in the present study. By enforcing the divergence-free condition, which is true for incompressible flows, we can reformulate Eq. (9) by:

$$\frac{\partial \Phi}{\partial t} + \nabla\cdot(\underline{u}\Phi) = \gamma\left[\nabla^2\Phi - \frac{\Phi(1-\Phi)(1-2\Phi)}{\epsilon^2} - |\nabla\Phi|\nabla\cdot\left(\frac{\nabla\Phi}{|\nabla\Phi|}\right)\right] \tag{15}$$

Now, the remaining thing is to collect the right-hand side of Eq. (15) as the conservative form. However, the present form of Eq. (15) cannot be collected as the conservative form. Thus Eq. (15) is reformulated as it's original form by using $\frac{(\nabla\Phi\cdot\nabla)|\nabla\Phi|}{|\nabla\Phi|} = \frac{\Phi(1-\Phi)(1-2\Phi)}{\epsilon^2}$

$$\frac{\partial \Phi}{\partial t} + (\underline{u}\cdot\nabla)\Phi = \gamma\left[\nabla^2\Phi - \frac{\nabla\Phi\cdot\nabla|\nabla\Phi|}{|\nabla\Phi|} - |\nabla\Phi|\nabla\cdot\left(\frac{\nabla\Phi}{|\nabla\Phi|}\right)\right] \tag{16}$$

Eq. (16) can then be derived as the following equation using $|\nabla\Phi| = \frac{\Phi(1-\Phi)}{\epsilon}$

$$\frac{\partial \Phi}{\partial t} + \nabla\cdot(\underline{u}\Phi) = \gamma\left[\nabla^2\Phi - \frac{\nabla\Phi}{|\nabla\Phi|}\cdot\nabla\left[\frac{\Phi(1-\Phi)}{\epsilon}\right] - \frac{\Phi(1-\Phi)}{\epsilon}\nabla\cdot\left(\frac{\nabla\Phi}{|\nabla\Phi|}\right)\right] \tag{17}$$

The last two terms in the right-hand side of Eq. (17) can be collected as $\nabla\cdot\left[\frac{\Phi(1-\Phi)}{\epsilon}\frac{\nabla\Phi}{|\nabla\Phi|}\right]$. The present conservative phase-field equation can be finally derived as

$$\frac{\partial \Phi}{\partial t} + \nabla\cdot(\underline{u}\Phi) = \bar{\gamma}\left(\epsilon\nabla\cdot(\nabla\Phi) - \nabla\cdot[\Phi(1-\Phi)\frac{\nabla\Phi}{|\nabla\Phi|}]\right) \tag{18}$$

where $\bar{\gamma} = \frac{\gamma}{\epsilon}$. In present study, unless we mention different values in the article, $\bar{\gamma}$ is chosen as $|\underline{u}_{max}|$, and ϵ is chosen as $0.7h$, where h is the mesh size. The second-order Runge–Kutta method is used for the temporal discretization.

It can be seen that all the terms shown in Eq. (18) are the same as ones in the conservative level set method (Eqs. (12) and (13)) if we using the definition $\underline{n} = \frac{\nabla\Phi}{|\nabla\Phi|}$. One can also see the present conservative phase-field method as a one-step conservative level set method. It can be expected that by using the present method, the mass can also be well conserved comparing with the original phase-field method due to its conservative form which is that same as the conservative level set method. The total mass can also be exactly conserved with the use of a conservative discretization. Moreover, the present method is more efficient than the original conservative level set method due to the fact that the proposed method is a one-step method which is that same as the phase-field method.

2.4. Dual-compact upwind advection scheme for the conservative phase-field equation

The dispersion-relation-preserving dual-compact upwind scheme have been proposed by the author [22]. Here we will briefly show the derivation.

Assume that the first derivative term $\frac{\partial\Phi}{\partial x}$ and the second derivative term $\frac{\partial^2\Phi}{\partial x^2}$, for example, in Eq. (18) are approximated respectively within the following three-point compact framework

$$a_1\frac{\partial\Phi}{\partial x}|_{i-1} + \frac{\partial\Phi}{\partial x}|_i = \frac{1}{h}(c_1\Phi_{i-1} + c_2\Phi_i + c_3\Phi_{i+1}) - h\left(b_1\frac{\partial^2\Phi}{\partial x^2}|_{i-1} + b_2\frac{\partial^2\Phi}{\partial x^2}|_i + b_3\frac{\partial^2\Phi}{\partial x^2}|_{i+1}\right) \tag{19}$$

$$\bar{b}_1\frac{\partial^2\Phi}{\partial x^2}|_{i-1} + \frac{\partial^2\Phi}{\partial x^2}|_i + \bar{b}_3\frac{\partial^2\Phi}{\partial x^2}|_{i+1} = \frac{1}{h^2}(\bar{c}_1\Phi_{i-1} + \bar{c}_2\Phi_i + \bar{c}_3\Phi_{i+1}) - \frac{1}{h}\left(\bar{a}_1\frac{\partial\Phi}{\partial x}|_{i-1} + \bar{a}_2\frac{\partial\Phi}{\partial x}|_i + \bar{a}_3\frac{\partial\Phi}{\partial x}|_{i+1}\right) \tag{20}$$

For terms $\frac{\partial\Phi}{\partial y}$ and $\frac{\partial^2\Phi}{\partial y^2}$, they can be similarly expressed along the y-direction. Note that the compact schemes for $\frac{\partial\Phi}{\partial x}|_i$ and $\frac{\partial^2\Phi}{\partial x^2}|_i$ are not independent of each other. They are rather strongly coupled through terms $\frac{\partial\Phi}{\partial x}|_{i-1}$, $\frac{\partial\Phi}{\partial x}|_i$, $\frac{\partial\Phi}{\partial x}|_{i+1}$, $\frac{\partial^2\Phi}{\partial x^2}|_{i-1}$, $\frac{\partial^2\Phi}{\partial x^2}|_i$, $\frac{\partial^2\Phi}{\partial x^2}|_{i+1}$, Φ_{i-1}, Φ_i and Φ_{i+1}. For the sake of description, we consider the above equation only for the case involving the positive convective coefficient.

Approximation of $\frac{\partial^2\Phi}{\partial x^2}$ can be normally made by applying the central schemes since the discretization error will be prevailingly dissipative. For this reason, the weighting coefficients shown in Eq. (20) will be determined solely by the modified equation analysis for rendering a higher spatial accuracy. Derivation of the coefficients $\bar{a}_1 \sim \bar{a}_3$, $\bar{b}_1$, $\bar{b}_3$ and $\bar{c}_1 \sim \bar{c}_3$ is as follows. We start by applying the Taylor series expansions for $\Phi_{i\pm1}$, $\frac{\partial\Phi}{\partial x}|_{i\pm1}$ and $\frac{\partial^2\Phi}{\partial x^2}|_{i\pm1}$ with respect to Φ_i, $\frac{\partial\Phi}{\partial x}|_i$ and $\frac{\partial^2\Phi}{\partial x^2}|_i$ and, then, eliminating the leading error terms derived in the modified equation. The coefficients of Eq. (20) can then be derived as $a_1 = -\frac{9}{8}$, $a_2 = 0$, $a_3 = \frac{9}{8}$, $b_1 = -\frac{1}{8}$, $b_3 = -\frac{1}{8}$, $c_1 = 3$, $c_2 = -6$, $c_3 = 3$.

Note that the coefficients shown above in Eq. (20) are exactly the same as those given in Chu and Fan [23]. It is also remarked that by virtue of the following derived modified equation, the presently derived coefficients can render the approximation of $\frac{\partial^2\Phi}{\partial x^2}$ with the spatial accuracy order of sixth as $\frac{\partial^2\Phi}{\partial x^2} = \frac{\partial^2\Phi}{\partial x^2}|_{exact} + \frac{h^6}{20160}\frac{\partial^8\Phi}{\partial x^8} + \frac{h^8}{604800}\frac{\partial^{10}\Phi}{\partial x^{10}} + O(h^{12}) + \cdots$.

The coefficients a_1, $b_1 \sim b_3$, $c_1 \sim c_3$ are partly determined by applying the Taylor series expansions for $\Phi_{i\pm1}$, $\frac{\partial\Phi}{\partial x}|_{i-1}$ and $\frac{\partial^2\Phi}{\partial x^2}|_{i\pm1}$ with respect to Φ_i, $\frac{\partial\Phi}{\partial x}|_i$ and $\frac{\partial^2\Phi}{\partial x^2}|_i$. We can then get the six equations, and it is still short of one algebraic equation for us to uniquely determine all the seven introduced coefficients shown in Eq. (19).

For physically accurate predicting the first derivative term from Eq. (19), the dispersive nature embedded in $\frac{\partial\Phi}{\partial x}$ must be retained as much as possible. The reason is that the dispersion relation governs the relation between the angular frequency and the wavenumber of the first-order dispersive term [27]. In other words, the solution can be accurately predicted as the dispersion relation is well preserved.

To preserve the dispersion relation, the Fourier transform and its inverse for Φ given below will be applied

$$\widetilde{\Phi}(\alpha) = \frac{1}{2\pi}\int_{-\infty}^{+\infty}\Phi(x)\ \exp(-\mathbf{i}\alpha x)dx, \tag{21}$$

$$\Phi(x) = \int_{-\infty}^{+\infty} \tilde{\Phi}(\alpha)\ \exp(\mathbf{i}\alpha x) d\alpha. \tag{22}$$

Note that the notation $\mathbf{i}$ shown above is equal to $\sqrt{-1}$. Development of the dispersion-relation preserving scheme is followed by performing Fourier transform on each term shown in Eqs. (19) and (20). The expressions of the actual wavenumber α for these two equations can be therefore derived as

$$\mathbf{i}\alpha h(a_1 \exp(-\mathbf{i}\alpha h) + 1) \simeq c_1 \exp(-\mathbf{i}\alpha h) + c_2 + c_3 \exp(\mathbf{i}\alpha h) - (\mathbf{i}\alpha h)^2 (b_1 \exp(-\mathbf{i}\alpha h) + b_2 + b_3 \exp(\mathbf{i}\alpha h)) \tag{23}$$

$$(\mathbf{i}\alpha h)^2 \left(-\frac{1}{8}\exp(-\mathbf{i}\alpha h) + 1 - \frac{1}{8}\exp(\mathbf{i}\alpha h)\right) \simeq 3\exp(-\mathbf{i}\alpha h) - 6 + 3\exp(\mathbf{i}\alpha h) - \mathbf{i}\alpha h\left(-\frac{8}{9}\exp(-\mathbf{i}\alpha h) + \frac{8}{9}\exp(\mathbf{i}\alpha h)\right) \tag{24}$$

In an approximation sense, the effective wavenumbers α' and α'' are derived to have the same expressions as those shown in the right-hand sides of Eqs. (23) and (24) [27]. For this reason, it is rational for us to express α' and α'' as follows:

$$\mathbf{i}\alpha' h(a_1 \exp(-\mathbf{i}\alpha h) + 1) = c_1 \exp(-\mathbf{i}\alpha h) + c_2 + c_3 \exp(\mathbf{i}\alpha h) - (\mathbf{i}\alpha'' h)^2 (b_1 \exp(-\mathbf{i}\alpha h) + b_2 + b_3 \exp(\mathbf{i}\alpha h)) \tag{25}$$

$$\mathbf{i}\alpha' h(-\frac{8}{9}\exp(-\mathbf{i}\alpha h) + \frac{8}{9}\exp(\mathbf{i}\alpha h)) = 3\exp(-\mathbf{i}\alpha h) - 6 + 3\exp(\mathbf{i}\alpha h) - (\mathbf{i}\alpha'' h)^2(-\frac{1}{8}\exp(-\mathbf{i}\alpha h) + 1 - \frac{1}{8}\exp(\mathbf{i}\alpha h)) \tag{26}$$

By solving Eqs. (25) and (26), the following expressions for α' and α'' can be derived

$$\begin{aligned}\alpha' h = {} & -\mathbf{i}(24b_1\exp(-2\mathbf{i}\alpha h) + c_1\exp(-2\mathbf{i}\alpha h) + c_3 + c1 + 24b_1 + c_2\exp(-\mathbf{i}\alpha h) + 24b_2\exp(-\mathbf{i}\alpha h) + 24b_3 \\ & - 48b_1\exp(-\mathbf{i}\alpha h) - 8c_1\exp(-\mathbf{i}\alpha h) - 48b_3\exp(\mathbf{i}\alpha h) + 24b_2\exp(\mathbf{i}\alpha h) + 24b_3\exp(2\mathbf{i}\alpha h) - 48b_2 + c_2\exp(\mathbf{i}\alpha h) \\ & + c_3\exp(2\mathbf{i}\alpha h) - 8c_3\exp(\mathbf{i}\alpha h) - 8c_2)/(-8 + \exp(\mathbf{i}\alpha h) - 8a_1\exp(-\mathbf{i}\alpha h) + a_1\exp(-2\mathbf{i}\alpha h) - 9b_1\exp(-2\mathbf{i}\alpha h) \\ & - 9b_2\exp(-\mathbf{i}\alpha h) + 9b_2\exp(\mathbf{i}\alpha h) + 9b_3\exp(2\mathbf{i}\alpha h) + a_1 + 9b_1 - 9b_3 + \exp(\mathbf{i}\alpha h))\end{aligned} \tag{27}$$

$$\alpha'' h = \sqrt{-\frac{3\exp(-\mathbf{i}\alpha h) - 6 + 3\exp(\mathbf{i}\alpha h) - \mathbf{i}\alpha' h(-\frac{8}{9}\exp(-\mathbf{i}\alpha h) + \frac{8}{9}\exp(\mathbf{i}\alpha h))}{-\frac{1}{8}\exp(-\mathbf{i}\alpha h) + 1 - \frac{1}{8}\exp(\mathbf{i}\alpha h)}} \tag{28}$$

For the sake of acquiring a better dispersive accuracy for α', it is demanded that $\alpha h \approx \Re[\alpha' h]$, where $\Re[\alpha' h]$ denotes the real part of $\alpha' h$. This implies that $E(\alpha)$ defined below should be a very small and positive value

$$E(\alpha) = \int_{-\frac{\pi}{2}}^{\frac{\pi}{2}} [W(\alpha h - \Re[\alpha' h])]^2 d(\alpha h) = \int_{-\frac{\pi}{2}}^{\frac{\pi}{2}} [W(\gamma - \Re[\gamma'])]^2 d\gamma \tag{29}$$

where $\gamma = \alpha h$, $\gamma' = \alpha' h$ and W is the weighting function which should be carefully chosen so that Eq. (29) can be analytically integrable. To make E defined in Eq. (29) to be positive and minimum, the following extreme condition is enforced

$$\frac{\partial E}{\partial c_3} = 0 \tag{30}$$

The above equation, which is enforced to preserve the dispersion relation, will be used together with another six previously derived algebraic equations by the modified equation analysis to acquire higher dissipation as well as the dispersion accuracies. The resulting seven introduced unknowns given below can be uniquely determined as $a_1 = 0.875$, $b_1 = 0.12512823415990895606$, $b_2 = -0.24871765840091043936$, $b_3 = 0.000128234159908956 0636$, $c_1 = -1.9359611900810925272$, $c_2 = 1.9969223801621850545$, $c_3 = -0.060961190081092527237$. We remark here that the above upwinding scheme developed for $\frac{\partial \Phi}{\partial x}$ can be easily shown to have the spatial accuracy order of fifth from the following modified equation $\frac{\partial \Phi}{\partial x} = \frac{\partial \Phi}{\partial x}|_{exact} - 0.00070085615243989 22475 h^5 \frac{\partial^6 \Phi}{\partial x^6} + 0.00019841269841269841 27 h^6 \frac{\partial^7 \Phi}{\partial x^7}$ $-0.00004988305074583303 90 h^7 \frac{\partial^8 \Phi}{\partial x^8} + O(h^8) + \cdots$. The reader can refer to [22] for the more details.

In order to conserve the total mass exactly, approximating the advection flux term $\frac{\partial (u\Phi)}{\partial x}$, for example, with a conservative form is necessarily. In the present study, we firstly approximate the half nodal values using the following equations

$$a_1 \Phi_{i-\frac{1}{2}} + \Phi_{i+\frac{1}{2}} = c_3 \Phi_{i+1} - c_1 \Phi_i - h\left(b_1 \frac{\partial \Phi}{\partial x}|_{i-\frac{1}{2}} + b_2 \frac{\partial \Phi}{\partial x}|_{i+\frac{1}{2}} + \frac{\partial \Phi}{\partial x}|_{i+\frac{3}{2}}\right) \tag{31}$$

$$\bar{b}_1 \frac{\partial \Phi}{\partial x}|_{i-\frac{1}{2}} + \frac{\partial \Phi}{\partial x}|_{i+\frac{1}{2}} + \bar{b}_3 \frac{\partial \Phi}{\partial x}|_{i+\frac{3}{2}} = \frac{1}{h^2}(\bar{c}_3 \Phi_{i+1} - \bar{c}_2 \Phi_i) - \frac{1}{h}\left(\bar{a}_1 \Phi_{i-\frac{1}{2}} + \bar{a}_2 \Phi_{i+\frac{1}{2}} + \bar{a}_3 \Phi_{i+\frac{3}{2}}\right) \tag{32}$$

After getting the half nodal values $\Phi_{i+\frac{1}{2}}$ and $\Phi_{i-\frac{1}{2}}$, one can then approximate the flux term for point i as

$$\frac{\partial (u\Phi)}{\partial x}|_i = \frac{u_{i+\frac{1}{2}} \Phi_{i+\frac{1}{2}} - u_{i-\frac{1}{2}} \Phi_{i-\frac{1}{2}}}{h} \tag{33}$$

2.5. Mass-redistribution method

Even use the high-resolution method or limiter, undershoot/overshoot values with small magnitude are still happened when solving the conservative phase-field equation. Also, due to the truncation error, the total mass will change with small

magnitude. In order to conserve the global mass exactly and eliminate the problem of undershoot/overshoot values, we propose the mass-redistribution method in the present study. The idea is to re-distribute the summation of the undershoot/overshoot and the loss/increase values in the transition region. Here is the summary for the mass-redistribution method.

(i) Filter the undershoot/overshoot values;

$$\Phi = \begin{cases} 1, \text{if } \Phi > 1 + 10^{-7} \\ 0, \text{if } \Phi < 10^{-7} \\ \Phi, \text{else} \end{cases} \tag{34}$$

(ii) Compute the total mass M at present time t;

$$M = \int_{\Omega} \Phi d\Omega \tag{35}$$

(iii) Compute the difference G for the mass between the initial time t_0 and present time t

$$G = M_0 - M \tag{36}$$

where $M_0 = \int_{\Omega} \Phi | t = 0 d\Omega$ is the total mass at initial time t_0.

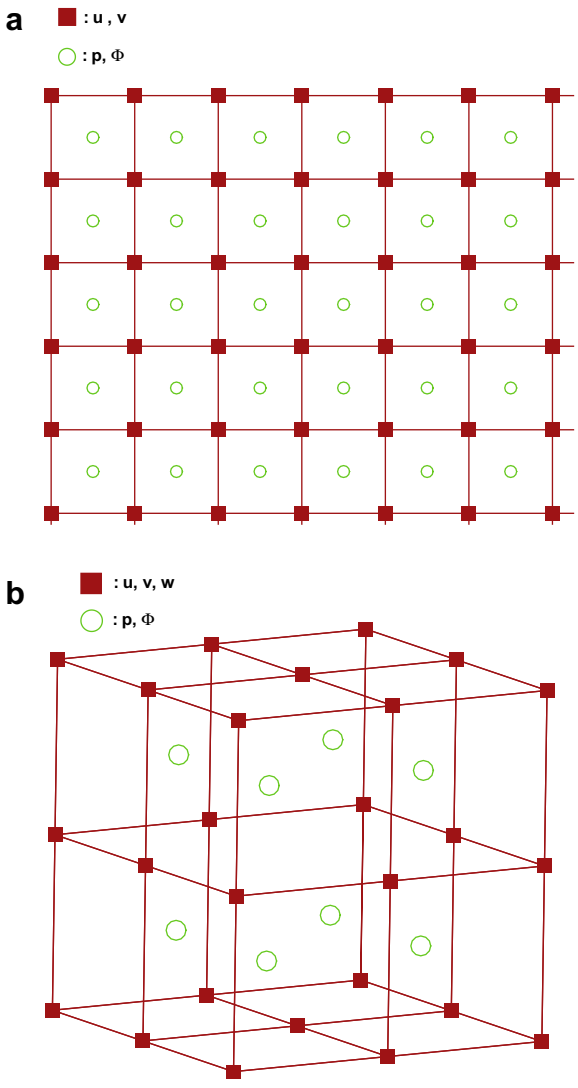

Fig. 1. Schematic for the present semi-stagger grid system. (a) two-dimensional; (b) three-dimensional.

(iv) Uniformly distribute G at N_G meshes as G/N_G, where N_G is the total numbers cells for the transition region ($0.001 < \Phi < 0.999$). By using the present method, the total mass can be exactly conserved. The undershoot/overshoot values can also be eliminated.

3. Two-phase flow solver

For two immiscible fluids which are considered to be incompressible, the equations of motion for this two-phase fluids in a gravitational vector field $\underline{g}$ can be represented by the incompressible flow equations given below:

$$\frac{\partial \underline{u}}{\partial t} + (\underline{u}\cdot\nabla)\underline{u} = \frac{1}{\rho}\left(-\nabla p + \nabla\cdot(2\mu\underline{\underline{D}}) + \underline{F_s} + \rho\underline{g}\right) \tag{37}$$

where ρ is the density, μ is the viscosity, $\underline{\underline{D}}$ is the rate of deformation tensor, p is the pressure, and the $\underline{F_s}$ is the surface tension force which is denoted as $\underline{F_s} = \sigma\kappa\delta\underline{n}$. The above equations can be casted in the dimensionless equations as

$$\frac{\partial \underline{u}}{\partial t} + (\underline{u}\cdot\nabla)\underline{u} = \frac{1}{\rho}\left(-\nabla p + \frac{1}{Re}\nabla\cdot(2\mu\underline{\underline{D}}) + \frac{1}{We}\underline{F_s}\right) + \frac{1}{Fr^2}\underline{e}_g \tag{38}$$

where $Re = \frac{\rho_r V_r L_r}{\mu_r}$ is the Reynolds number, $We = \frac{\rho_r V_r^2 L_r}{\sigma}$ is the Weber number and the $Fr = \frac{V_r}{\sqrt{gL_r}}$ is the Froude number. The density and viscosity are approximated as $\rho = \rho_{GL} + (1-\rho_{GL})\Phi$ and $\mu = \mu_{GL} + (1-\mu_{GL})\Phi$, where ρ_{GL} and μ_{GL} are the ratios for the density and viscosity.

3.1. Semi-implicit Gear scheme and projection method

In present study, the momentum equations are discretized by the Gear scheme as:

$$\begin{aligned}\frac{3\underline{u}^{n+1,*} - 4\underline{u}^{n} + \underline{u}^{n-1}}{2\Delta t} = {} & -2[(\underline{u}\cdot\nabla)\underline{u}]^{n} + [(\underline{u}\cdot\nabla)\underline{u}]^{n-1} + 2\frac{1}{\rho^{n+1}}\left[\frac{1}{Re}\nabla\cdot(2\mu\underline{\underline{D}} - \nabla^2\underline{u})\right]^{n} \\ & - \frac{1}{\rho^{n+1}}\left[\frac{1}{Re}\nabla\cdot(2\mu\underline{\underline{D}} - \nabla^2\underline{u})\right]^{n-1} + \left(\left(\frac{1}{\rho}\left(-\nabla p + \frac{1}{Re}\nabla^2\underline{u} + \frac{1}{We}\underline{F_s}\right) + \frac{1}{Fr^2}\underline{e}_g\right)^{n+1,*}\right.\end{aligned} \tag{39}$$

the above equation can be collected as a Helmholtz equation as the form $(\mathbf{I} + \mathbf{A})\underline{u}^{n+1} = \mathbf{F}$, and solved by the standard iterative scheme such as successive overrelaxation (SOR) method. No non-linear iteration is needed for the present semi-implicit scheme.

The intermediate velocity $\underline{u}^{n+1,*}$ is generally not divergence-free. It is then proposed the following pressure correction equation in order to satisfy the divergence-free condition:

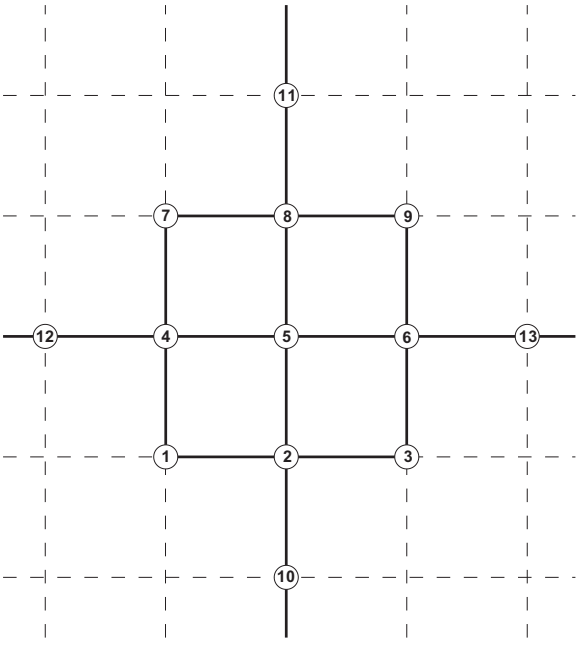

Fig. 2. Schematic of the stencil points invoked in the proposed two-dimensional DRP convection scheme.

$$\frac{3(\underline{u}^{n+1}-\underline{u}^{n+1,*})}{2\Delta t}=-\frac{1}{\rho}\nabla p' \tag{40}$$

$$p^{n+1}=p^{n+1,*}+p' \tag{41}$$

Take the divergence on Eq. (40), the following Poisson equation for the pressure correction can be derived

$$\nabla\cdot\left(\frac{1}{\rho}\nabla p'\right)=\frac{3(\nabla\cdot\underline{u}^{n+1,*})}{2\Delta t} \tag{42}$$

After solving Eq. (42), one can get the corrected velocity $\underline{u}^{n+1}=\underline{u}^{n+1,*}-\frac{2}{3}\Delta t\left(\frac{1}{\rho}\nabla p'\right)$, and the corrected pressure $p^{n+1}=p^{n+1,*}+p'$.

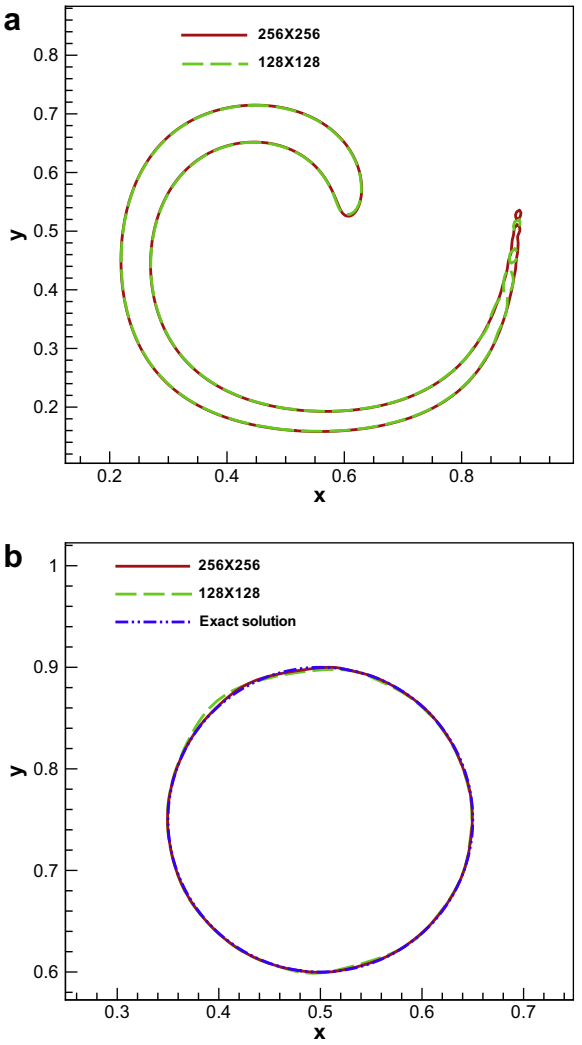

Fig. 3. The predicted results using the current conservative phase-field method for the reversed single vortex problem. (a) $t=2$; (b) $t=4$.

Table 1
The predicted spatial rates of convergence for the test problem given in Section 4.1.

Mesh size	1/32	1/64	1/128	1/256
Errors	2.322E−2	5.673E−3	1.237E−3	4.490E−4
Rate of convergence	–	2.033	2.196	1.462

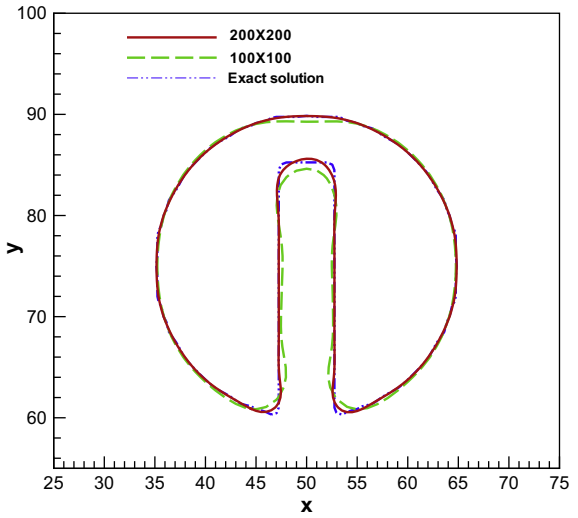

Fig. 4. The predicted results using the current conservative phase-field method with 100 × 100 and 200 × 200 meshes for the Zalesak's test problem.

3.2. Multi-dimensional advection scheme for advection terms

We present in the subsection the way of approximating $\underline{u}_x$, which can accommodate the dispersion-relation-preserving property. Referring to Fig. 1, $\underline{u}_x$ at the nodal point (i,j) under $\Delta x = \Delta y = h$ is assumed to be expressed as

$$\underline{u}_x(x,y) \simeq \frac{1}{h}\left(d_1\underline{u}_{i-1\,j-1} + d_2\underline{u}_{i\,j-1} + d_3\underline{u}_{i+1\,j-1} + d_4\underline{u}_{i-1\,j} + d_5\underline{u}_{i\,j} + d_6\underline{u}_{i+1\,j} + d_7\underline{u}_{i-1\,j+1} + d_8\underline{u}_{i\,j+1} + d_9\underline{u}_{i+1\,j+1} + d_{10}\underline{u}_{i\,j-2} + d_{11}\underline{u}_{i\,j+2} + d_{12}\underline{u}_{i-2\,j}\right) \tag{43}$$

By substitution of the Taylor series expansions for $\underline{u}_{i\pm1\,j}$, $\underline{u}_{i_{-2}\,j}$, $\underline{u}_{i\,j\pm1}$, $\underline{u}_{i\,j\pm2}$, $\underline{u}_{i\pm1\,j\pm1}$ into the above equation, we are led to derive the resulting modified equation for $\underline{u}_x$. The derivation is followed by eliminating eleven leading error terms to yield a system of eleven algebraic equations. One more equation has to be derived so as to be able to uniquely determine $d_1 \sim d_{12}$ shown in Eq. (43). By solving all the equations with the dispersion-relation-preserving equation, we can obtain the following coefficients $d_1 = d_3 = d_7 = d_9 = 0$, $d_2 = d_8 = \frac{1}{9}\frac{\pi(3\pi-10)}{(3\pi-8)}$, $d_4 = -1$, $d_6 = \frac{1}{3}$, $d_5 = \frac{1}{6}\frac{3\pi^2-19\pi+24}{(3\pi-8)}$, $d_{10} = a_{11} = -\frac{1}{36}\frac{\pi(3\pi-10)}{(3\pi-8)}$, and $d_{12} = \frac{1}{6}$. In the resulting modified equation, $\underline{u}_x$ is shown to have a spatial accuracy order of three in the sense that $\underline{u}_x \simeq \frac{h^3}{12}\underline{u}_{xxxx} + \frac{h^3}{18}\frac{\pi(3\pi-10)}{(\pi^2-6\pi+8)}\underline{u}_{yyyy} - \frac{h^4}{30}\underline{u}_{xxxxx} + \frac{h^5}{72}\underline{u}_{xxxxxx} + \cdots$. For the details of derivations, the reader can refer to [28].

3.3. Velocity–pressure coupling

When solving the incompressible flow equation, special care must be taken for the coupling with velocity and pressure. If one uses the non-staggered grids, simply using the standard central difference for approximating pressure gradient will lead to a unphysical distribution for the pressure field. While the odd–even decoupling problem can be eliminated on the staggered grid, the resulting programming complexity is still a main task. In the present study, a semi-staggered grid is used for coupling the velocity and pressure [26]. The velocity vectors are stored at the cell edge, the pressure and other scalar fields are stored at the cell center, as shown in Fig. 2. For this grid system, the programming is much simpler than staggered grid system, and the coupling can be easily achieved if one employs a pressure interpolation from cell center to cell edge.

3.4. Continuum surface force model and Helmholtz smoother

In present study, the surface tension force is approximated using the continuum surface force model (CSF) [24] as $\underline{F}_s = \sigma\widetilde{\kappa}\nabla\widetilde{\Phi}$. For this approach, how to calculate the curvature term $\widetilde{\kappa}$ is one main issue. In order to get a better representation for the curvature, one can use the smoothing kernel function [25]. Instead of using the smoothing kernel function, we use the Helmholtz smoother in this study. With the definition of the Helmholtz operator

$$\mathbf{H} = 1 - \epsilon^2\nabla^2 \tag{44}$$

we can calculate the smoothed value $\widetilde{\Phi}$ by the following Helmholtz equation $\Phi = \mathbf{H}\widetilde{\Phi}$ as

$$\Phi = \widetilde{\Phi} - \epsilon^2\nabla^2\widetilde{\Phi} \tag{45}$$

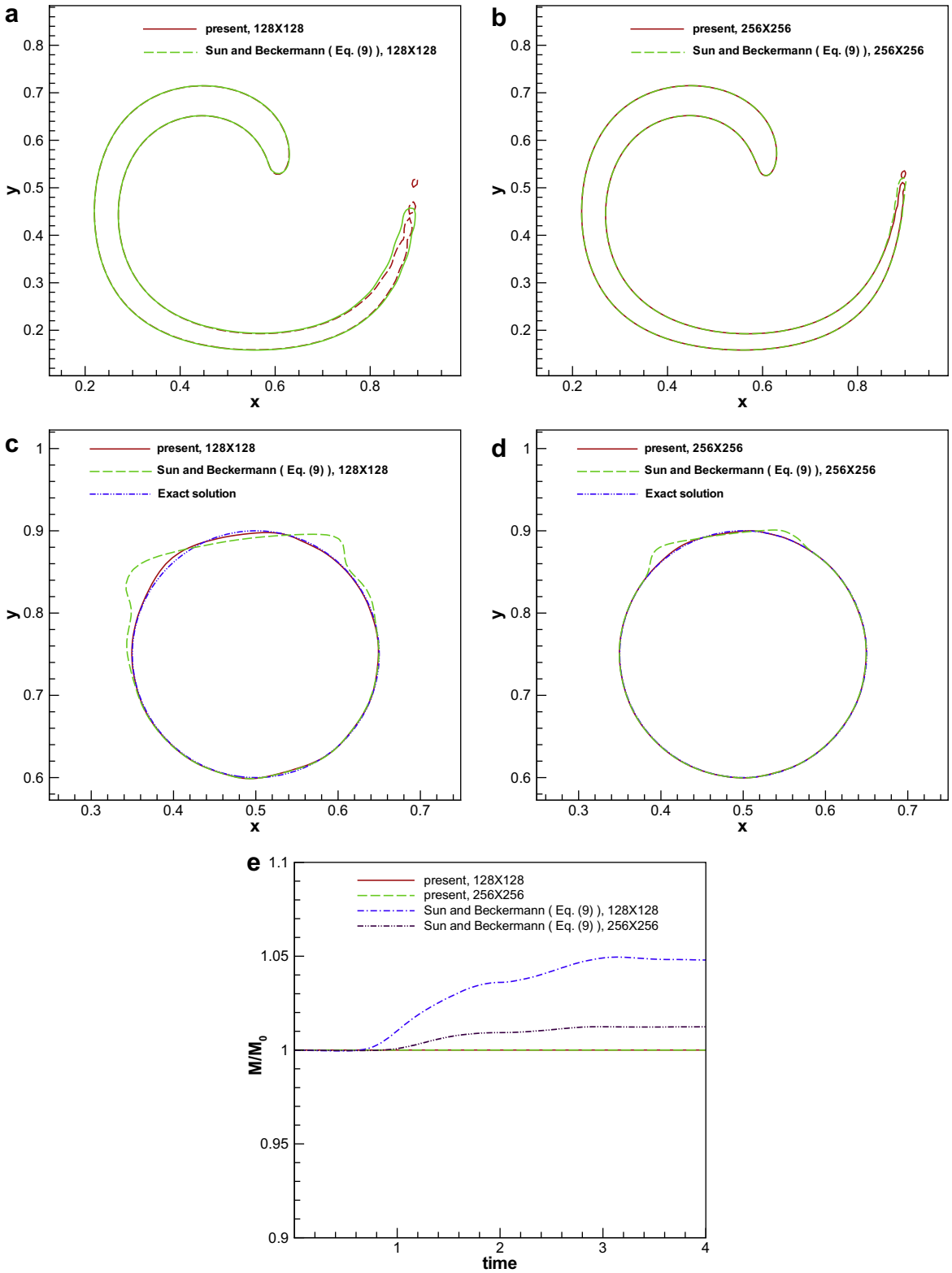

Fig. 5. Comparison of present method and the phase field method of Sun and Beckermann [15] for the reversed single vortex problem. (a–b) $t = 2$; (c–d) $t = 4$; (e) the predicted total mass ratios against time. Note that $M = \int_\Omega \Phi d\Omega$ means the total mass and $M_0 = \int_\Omega \Phi|_{t=0} d\Omega$ means the total mass at $t = 0$.

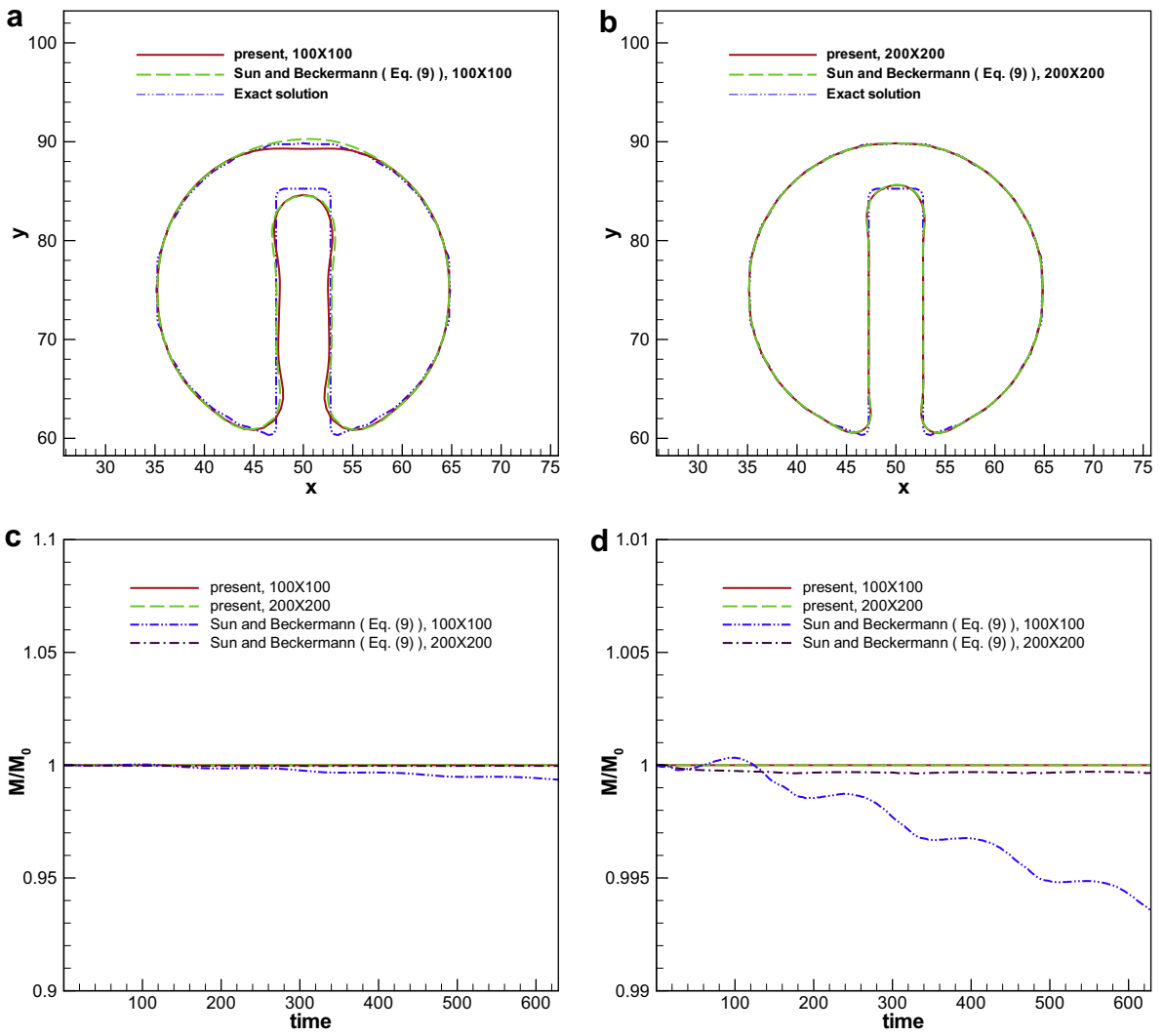

Fig. 6. Comparison of present method and the phase field method of Sun and Beckermann [15] for the reversed single vortex problem. (a) 100×100 meshes; (b) 200×200 meshes; (c) the predicted total mass ratios against time; (d) close view of (c). Note that $M = \int_\Omega \Phi d\Omega$ means the total mass and $M_0 = \int_\Omega \Phi|_{t=0} d\Omega$ means the total mass at $t = 0$.

the curvature term can then be calculated by $\widetilde{\Phi}$ as

$$\kappa = \nabla \cdot \left(\frac{\nabla \widetilde{\Phi}}{|\nabla \widetilde{\Phi}|} \right) \tag{46}$$

Note that this kind of Leray-type smoothed operator [29] has been recently proposed for its role of regularizing the inviscid Burgers equation.

4. Verification studies

4.1. Reversed single vortex problem

The reversed single vortex problem [30] is simulated for the present conservative phase-field method. In this problem, a circle is located at (0.5,0.75) in a unit computational domain $[0,1] \times [0,1]$. The velocities are defined by the following streamfunction:

$$\Psi = \frac{1}{\pi} \sin(\pi x)^2 \sin(\pi y)^2 \cos(\pi t/T) \tag{47}$$

$$u = \frac{-\partial\psi}{\partial x} \tag{48}$$

$$v = \frac{\partial\psi}{\partial y} \tag{49}$$

It is expected that when $t = T$, the circle will come back to its original position. In this study, we set $T = 4$, $\Delta t = \Delta x/8$, and $\bar{\gamma} = 0.5|u|$. The predicted solutions with 128×128 and 256×256 meshes are plotted in Fig. (3). From the figure, it can be seen that the present method can perform very well. The results of error and the corresponding rates of convergence are tabulated in Table 1, where the errors are defined as $\Sigma_{i,j}|\Phi(i,j) - \Phi^{exact}(i,j)|\Delta x\Delta y$. It shows that the rate of convergence is about 2 for the present method.

4.2. Zalesak's test problem

The Zalesak's test problem [31] have been known to be a good test problem for showing a scheme's performance. In this problem a circle with a notched width of 15, is rotated with a velocity field $u = \frac{\pi(50-y)}{314}$, $v = \frac{\pi(x-50)}{314}$. We simulated this problem

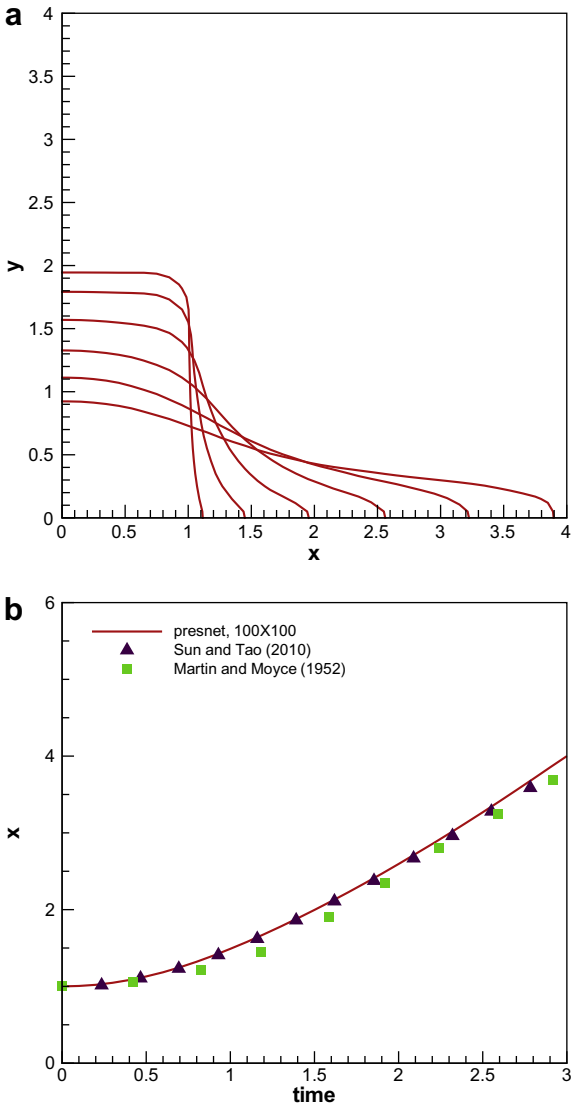

Fig. 7. Calculated results for the dam-break problem. (a) the time-history front profile; (b) Comparisons of the predicted front locations with the experimental data [32] and the numerical results [10].

with 100×100 and 200×200 meshes and $\Delta t = \Delta x/4$. Note that in this problem we set $\bar{\gamma} = 0.5|u|$. From the Fig. 4, good agreements with the exact solution schematic in the same figure are clearly confirmed. The applicability of the present scheme is then validated.

In order to show the advantage of the present method, The phase-field equation of Sun and Beckermann [15] (Eq. (9)) is also implemented for comparison purpose. From Figs. 5 and 6, it can be easily seen that the present method can conserve the total mass exactly, while the phase-field equation proposed in [15] cannot conserve the total mass. Furthermore, It can be

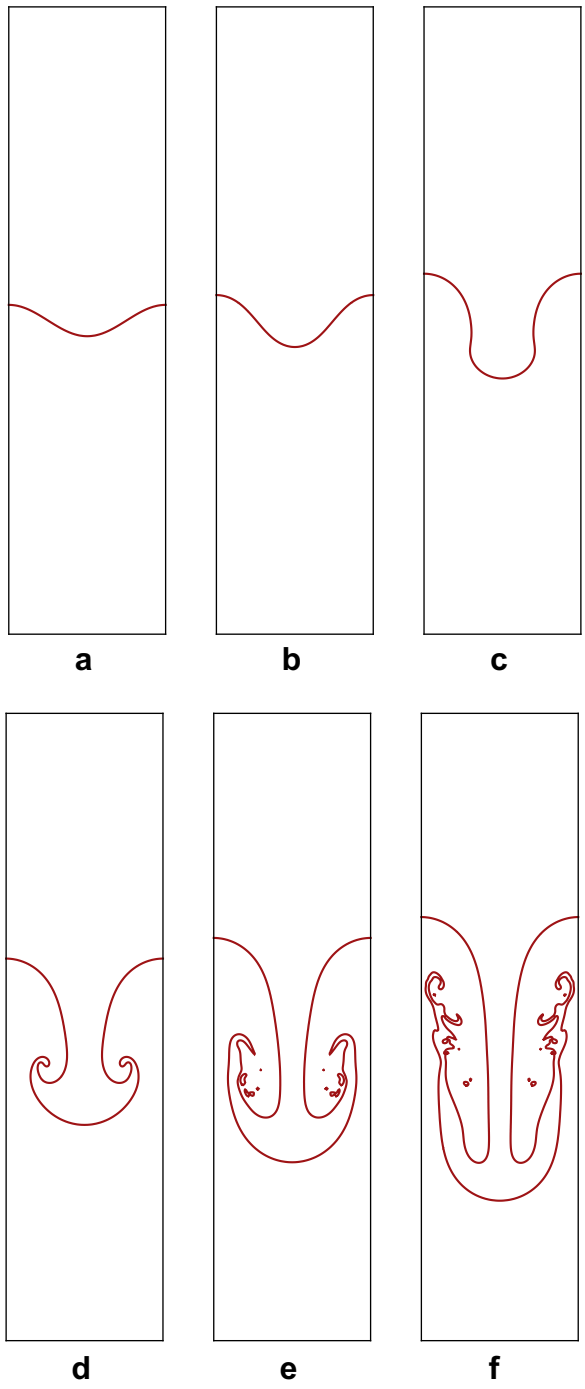

Fig. 8. The predicted time-evolving free surfaces for the Rayleigh–Taylor instability problem at different time. (a) $t = 0.0$; (b) $t = 0.5$; (c) $t = 1.0$; (d) $t = 1.5$ (e) $t = 2.0$; (f) $t = 2.5$.

shown that the present method can get better results. The accuracy and efficiency of the proposed conservative phase-field equation are thus validated again.

5. Numerical results

In this section, we will show the applicability of the present conservative phase-field method for solving the incompressible two-phase flows. For all investigated problems, no flux boundary conditions are used for the conservative phase-field equation, while slip-boundary conditions are used for the momentum equations.

5.1. Dam-break problem

This classical problem, known as the dam break problem, has been frequently employed to validate the code for predicting free surface hydrodynamics. In the current calculation, the fluid properties is the same as Martin and Moyce used in [32]. The initially prescribed width (L) and height (2L) of the water column are 0.146 m and 0.292 m, respectively. The liquid density $\rho_L = 10^3$ kg/m^3, viscosity μ_L=0.5 Pa s, background gas density ρ_G=1.0 kg/m^3, viscosity μ_G=0.5 $\times$ 10^3 Pa s, gravity g=9.8 m/s^2 and the surface tension coefficient σ=0.0755 N/m. By choosing the reference velocity as $\sqrt{g(2L)}$, it will lead to Re = 493.954, Fr = 1.414, We = 5533.690, ρ_{GL} = 0.001 and μ_{GL} = 0.001. 100 $\times$ 100 meshes are used for this calculation. Good

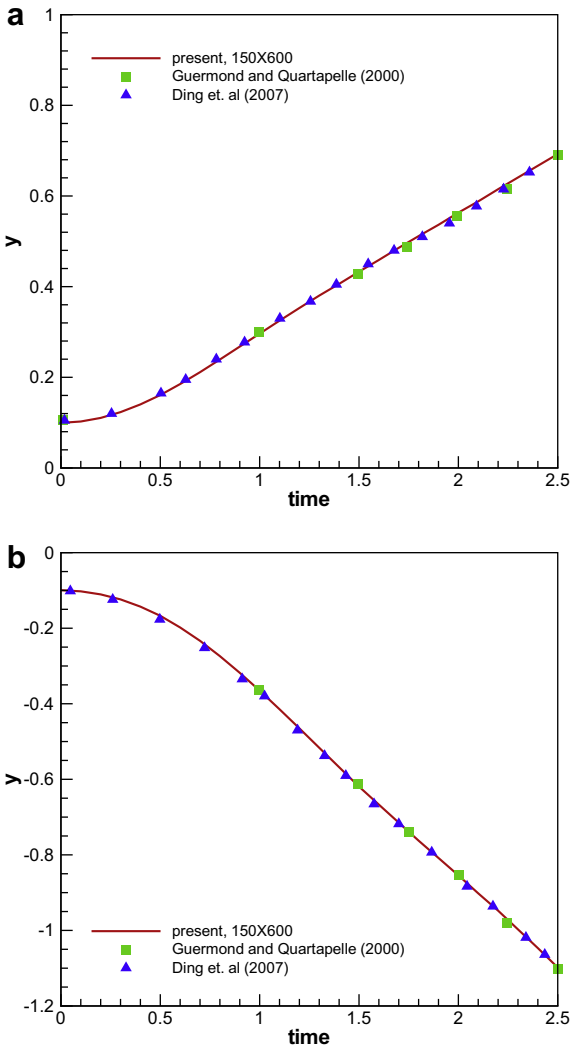

Fig. 9. Comparisons of the top of the rising fluid and the bottom of the falling fluid for the Rayleigh–Taylor instability problem. (a) rising fluid interface; (b) falling fluid interface.

agreements with the experimental results given in [32] and numerical results given in [10] are clearly demonstrated in Fig. 7 for the predicted front location.

5.2. Rayleigh–Taylor instability problem

Flow instability of the Rayleigh–Taylor type is associated with the penetration of a heavy fluid into a light fluid in the direction of gravity. The interface is given by $y(x) = (2D + 0.1D\ cos(2\pi x/D))$ in the rectangular domain $[0,D] \times [0,4D]$, where $D = 1$. The Reynolds number Re under investigation is 3000. The density difference is represented by the Atwood number $At = (\rho_L - \rho_G/\rho_L + \rho_G) = 0.5$ and the viscosity ratio is 1.$\bar{\gamma}$ is set as $|\underline{u}|$. Surface tension force is ignored for this problem. The predicted interface profiles with 150×600 meshes are given in Fig. 8. We also compare the top of the rising fluid and the bottom of the falling fluid with the solutions of Guermond et al.[33] and Ding et al.[16]. From the Fig. 9, The present method is justified by the good agreements between our solutions and previous studies obtained by [33,16].

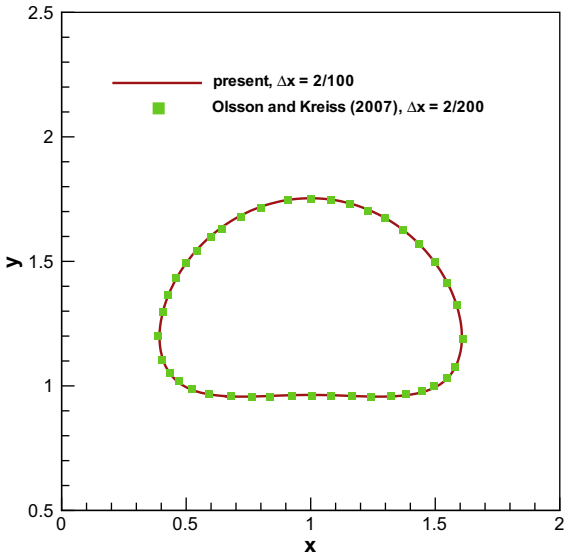

Fig. 10. Comparison of the bubble shape for the present method and solution obtained by Olsson and Kreiss [11].

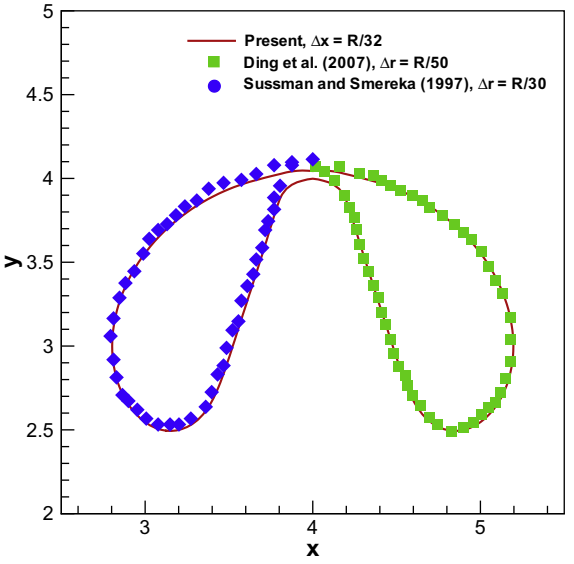

Fig. 11. Comparison of the bubble shape for the present method and solution obtained by Ding et al. [16] and Sussman and Smereka [5].

5.3. Bubble rising problem

The bubble rising problems are also known to be a good example for testing the accuracy and the efficiency for the numerical schemes. Here we investigate two bubble rising problem, one is a 2D cylindrical bubble, and the other is a 3D spherical bubble. For the 2D problem, there is a cylindrical bubble with diameter $D(=1)$ in the rectangular domain

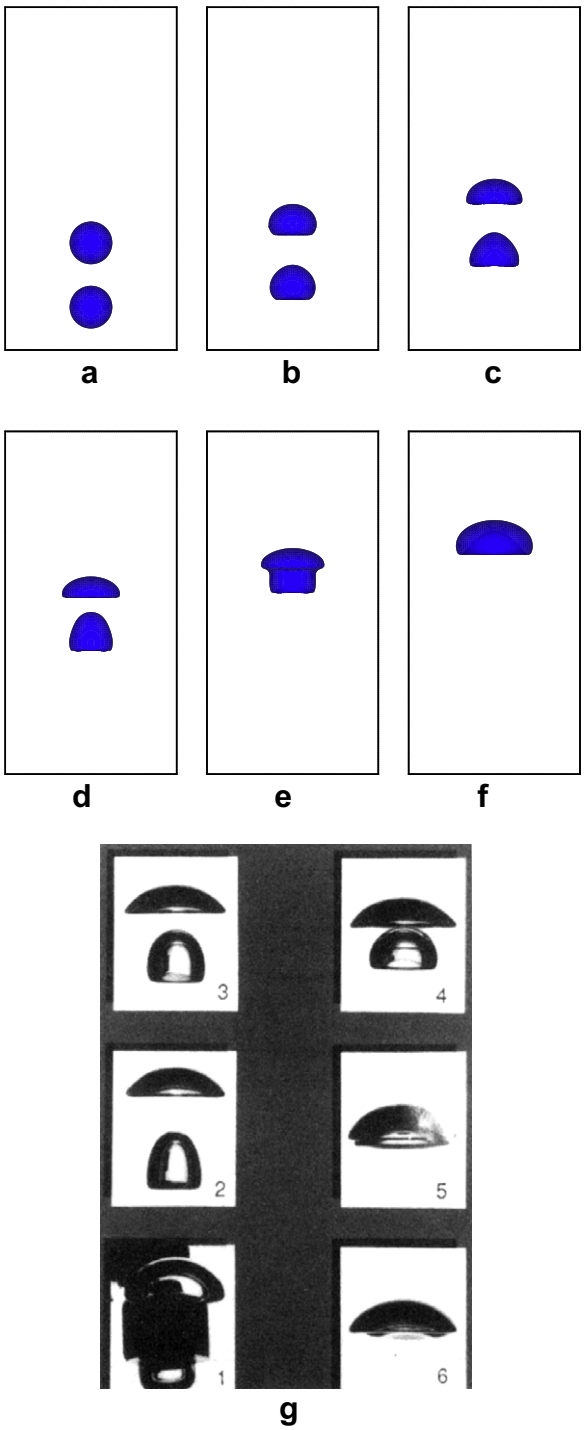

Fig. 12. Comparisons of the bubble shapes for the present method and experimental results (time difference between subsequent photographs is 0.03 s). (a) $t = 0.0$ s; (b) $t = 0.03$ s; (c) $t = 0.06$ s; (d) $t = 0.09$ s; (e) $t = 0.12$ s; (f) $t = 0.15$ s; (g) experimental results by Brereton and Korotney [34].

$[0,D] \times [0,2D]$. The Reynolds number is 500, Weber number is 0.68, and the Froude number is 0.45. The ratios for density and viscosity are $\rho_{GL} = 0.0013$ and $\mu_{GL} = 0.016$. A mesh of 50×100 is used for this problem. Comparison of the interface profile is made at $t = 0.5$. From the Fig. 10, the present results and the results obtained by Olsson and Kreiss [11] are matched very nicely.

After the success of the simulating two-dimensional case, we are now going to simulate the 3D-dimensional spherical bubble rising problem. The problem setting is the same as Ding et al. [16] and Sussman and Smereka[5]: There is a spherical bubble with radius $R(=1)$ in the cubic domain $[0,8R] \times [0,8R] \times [0,8R]$. The Reynolds number is 100, Weber number is 200, and the Froude number is 1. The ratios for density and viscosity are $\rho_{GL} = 0.001$ and $\mu_{GL} = 0.01$, respectively. Due to the fact that they solve the axisymmetric problem, we only compare the interface profile at the midplane. For the mesh size $\Delta x = \Delta y = \Delta z = R/32$, the predicted interface profile at $t = 1.6$ is shown in Fig. 11. Again, good agreements are obtained between the present result and the previous studies [16,5].

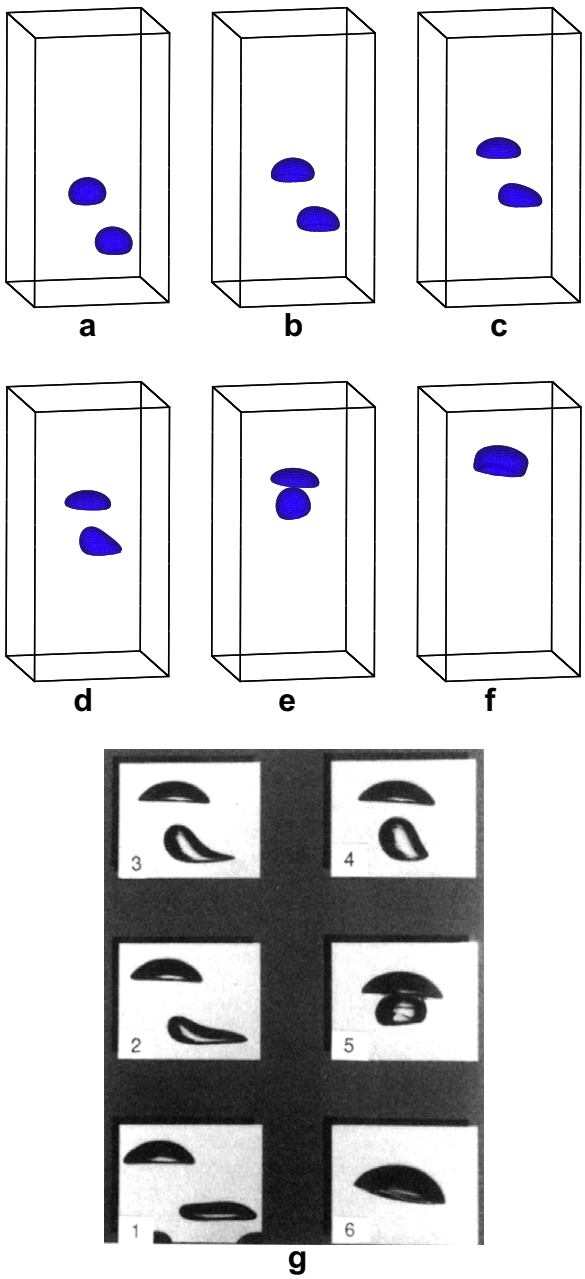

Fig. 13. Comparisons of the bubble shapes for the present method and experimental results (time difference between subsequent photographs is 0.03 s). (a) $t = 0.03$ s; (b) $t = 0.06$ s; (c) $t = 0.09$ s; (d) $t = 0.12$ s; (e) $t = 0.15$ s; (f) $t = 0.18$ s; (g) experimental results by Brereton and Korotney [34].

5.4. Bubble merging problem

The bubble merging problems with coaxial coalescence and oblique coalescence are considered here. There are two spherical bubbles with radius R(=1) in the cubic domain $[0,4R] \times [0,4R] \times [0,8R]$. For the coaxial problem, The center of upper bubble is at $(2R,2R,2.5R)$ and the center of lower bubble is at $(2R,2R,1R)$; for the oblique problem, The center of upper bubble is at $(2R,2R,2.5R)$ and the center of lower bubble is at $(2.85R,2R,1R)$. The Eotvos number ($Eo = \frac{\rho_T g L_T^2}{\sigma}$) is 16, and the Morten number $\left(Mo = \frac{g\mu_T^4}{\rho_T \sigma^3}\right)$ is 2×10^{-4}. This will lead Reynolds number equal to 67.27, Weber number equal to 16, and the Froude number equal to 1. The ratios for density and viscosity are $\rho_{GL} = 0.001$ and $\mu_{GL} = 0.01$, respectively. The time-history solutions obtained by $80 \times 80 \times 160$ meshes for different physical time are plotted in Figs. 12 and 13. The agreements with the experimental observations by Brereton and Korotney [34] can be shown for the present solutions.

For the sake of completeness, we also plot the ratio of the total mass against time for the bubble rising and merging problems. From Fig. 14, it can be seen again that the total mass can be conserved very well.

5.5. Milkcrown problem

Finally, The milkcrown problem is simulated in order to show the applicability of dealing with the complex topology changing problem for the present framework. Numerical simulations for this problem have been done by many researchers

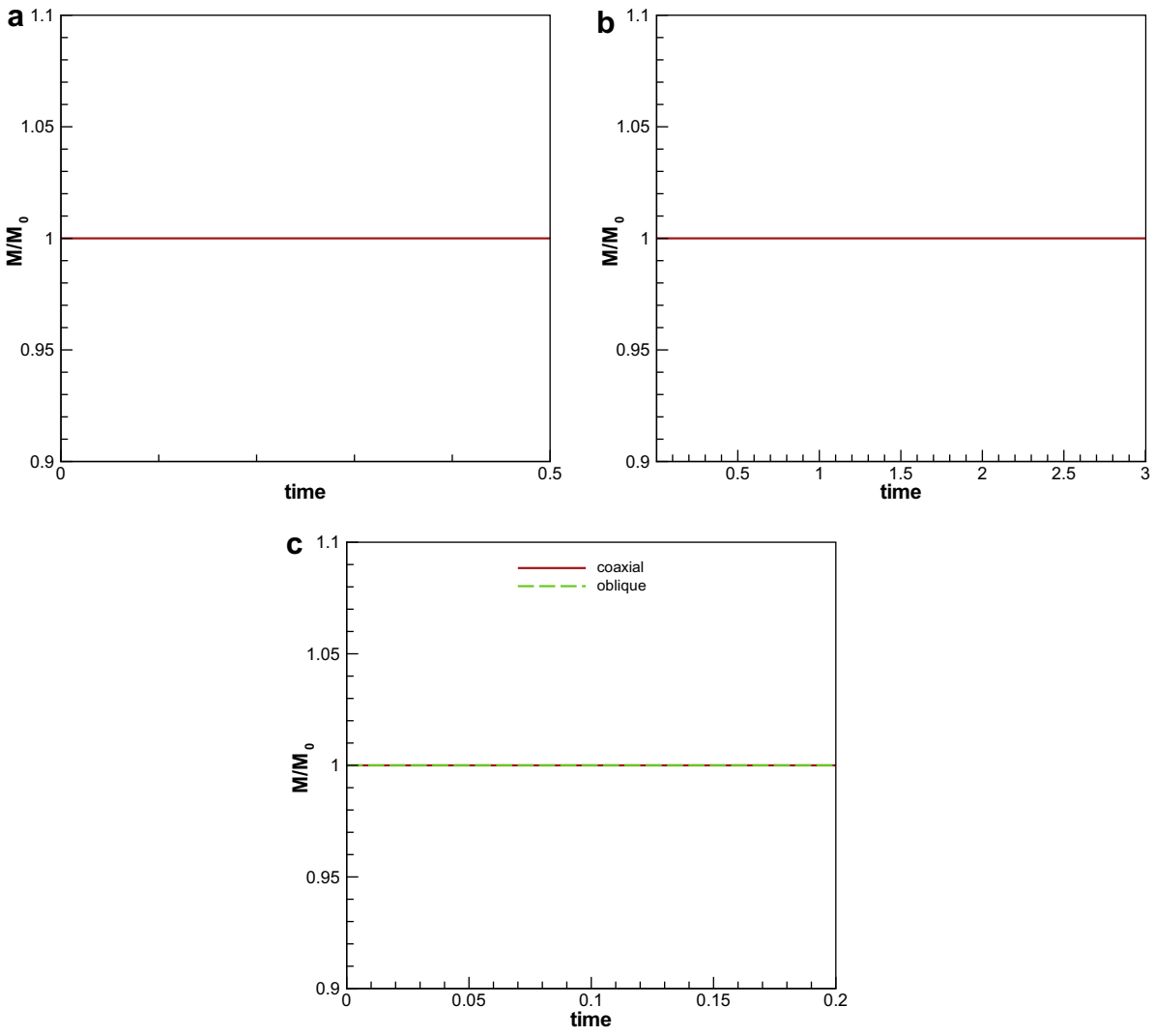

Fig. 14. The predicted total mass ratios against time for the investigated problems. (a) the 2D cylindrical bubble rising problem; (b) the 3D spherical bubble rising problem; (c) the bubble merging problems. Note that $M = \int_\Omega \Phi d\Omega$ means the total mass and $M_0 = \int_\Omega \Phi|_{t=0} d\Omega$ means the total mass at $t = 0$.

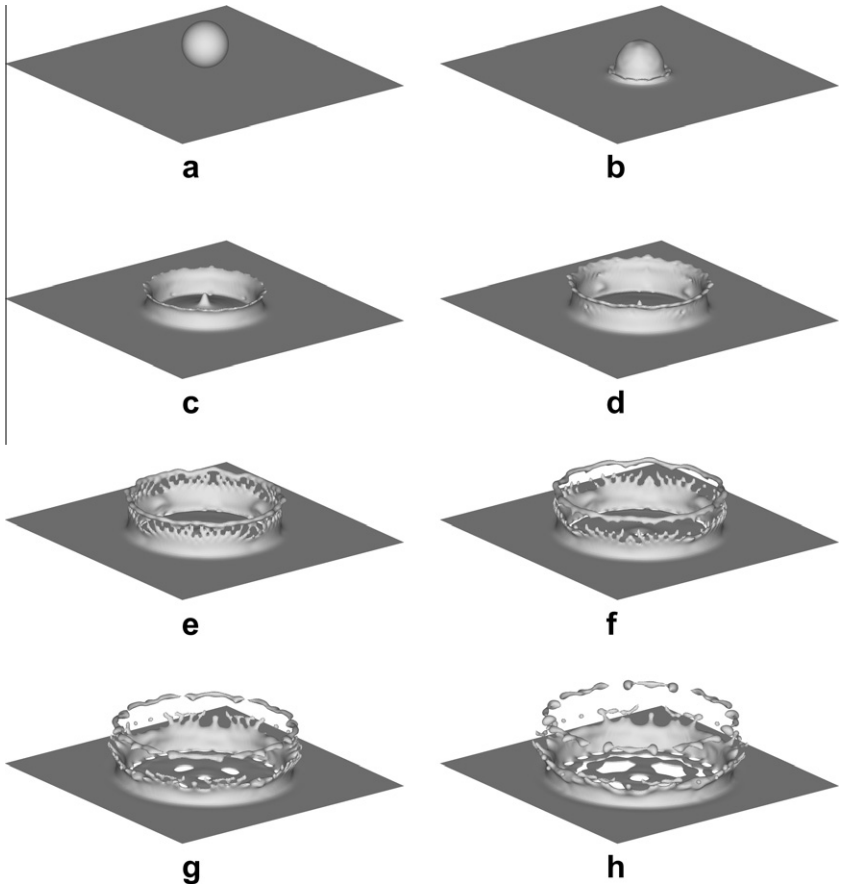

Fig. 15. The predicted time-evolving free surfaces, obtained at $200 \times 200 \times 100$ meshes, for the milkcrown problem at different time. (a) $t = 0.0$; (b) $t = 0.5$; (c) $t = 1.5$; (d) $t = 2.0$ (e) $t = 2.5$; (f) $t = 3.0$; (g) $t = 3.5$; (h) $t = 4.0$.

in 2D [35] and 3D [36–38]. In this study, we use the same setting as in [38]: There is a droplet with 5.33 mm diameter, fallen down with velocity 2 m/s into a liquid thin film with 1 mm depth. The densities for the liquid and air are 1000 kg/m^3 and 1.25 kg/m^3, the viscosities for the liquid and air are 1.7×10^{-3} Pa s and 1×10^{-6} Pa s. The surface tension coefficient σ is 5×10^{-2} N/m and the gravity g is 9.8 m/s^2. By using the above parameters, we can get the following non-dimensional numbers: $Re = 6270.588$, $Fr = 8.7509$, $We = 426$, $\rho_{GL} = \frac{1}{800}$ and $\mu_{GL} = \frac{1}{1700}$. We simulate this problem with $200 \times 200 \times 100$ meshes, which lead to $\Delta x = \Delta y = \Delta z \approx D/33$, where D is the diameter of the droplet. The predicted results are shown in Fig. 15. Good agreements can be observed for the present solutions and the results in [38].

6. Concluding remarks

A conservative phase-field method for modelling the incompressible two-phase flow is proposed. The present method is based on the work of Sun and Beckermann [15], which is motivated by the Allen–Cahn equation. The mass conservation can be exactly satisfied by the present framework. Both of the proposed dispersion-relation-preserving dual-compact upwind advection scheme and multi-dimensional dispersion-relation-preserving upwind scheme have shown to be robust for the present two-phase solver. Also, five benchmark problems with/without consideration of surface tension have been numerically investigated. All predicted results have been shown to compare fairly well with the benchmark, experimental and other numerical results.

Acknowledgements

We thank Kensuke Yokoi, Long Lee and Tony Wen-Hann Sheu for useful discussions, comments and supports.

References

[1] C.R. Anderson, A vortex method for flows with slight density variations, J. Comput. Phys. 61 (1985) 417–444.
[2] J.M. Boultone-Stone, J.R. Blake, Gas bubbles bursting at a free surface, J. Fluid Mech. 254 (1993) 437–466.

[3] C.W. Hirt, B.D. Nichols, Volume of fluid method (VOF) for the dynamics of free boundaries, J. Comput. Phys. 39 (1981) 201–225.
[4] S. Unverdi, G. Tryggvason, A front-tracking method for viscous, incompressible, multi-fluid flows, J. Comput. Phys. 100 (1992) 25–37.
[5] M. Sussman, P. Smereka, Axisymmetric free boundary problems, J. Fluid Mech. 341 (1997) 269–294.
[6] J.A. Sethian, Peter Smereka, Level set methods for fluid interfaces, Annu. Rev. Fluid Mech. 35 (2003) 341–372.
[7] M. Sussman, E.G. Puckett, A coupled level set and volume-of-fluid method for computing 3D and axisymmetric incompressible two-phase flows, J. Comput. Phys. 162 (2000) 301–337.
[8] F. Xiao, Y. Honma, T. Kono, A simple algebraic interface capturing scheme using hyperbolic tangent function, Int. J. Numer. Meth. Fluid 48 (2005) 1023–1040.
[9] Kensuke Yokoi, Efficient implementation of THINC scheme: a simple and practical smoothed VOF algorithm, J. Comput. Phys. 226 (2007) 1985–2002.
[10] D.L. Sun, W.Q. Tao, A coupled volume-of-fluid and level set (VOSET) method for computing incompressible two-phase flows, Int. J. Heat Mass Transfer 53 (2010) 645–655.
[11] E. Olsson, G. Kreiss, A conservative level set method for two phase flow, J. Comput. Phys. 210 (2005) 225–246.
[12] D.M. Anderson, G.B. McFadden, A.A. Wheeler, Diffuse-interface methods in fluid mechanics, Ann. Rev. Fluid Mech. 30 (1998) 139–165.
[13] V.E. Badalassi, H.D. Ceniceros, S. Banerjee, Computation of multiphase systems with phase field models, J. Comput. Phys. 190 (2003) 371–397.
[14] Junseok Kim, A continuous surface tension force formulation for diffuse-interface models, J. Comput. Phys. 204 (2005) 784–804.
[15] Y. Sun, C. Beckermann, Sharp interface tracking using the phase-field equation, J. Comput. Phys. 220 (2007) 626–653.
[16] H. Ding, Peter D.M. Spelt, C. Shu, Diffuse interface model for incompressible two-phase flows with large density ratios, J. Comput. Phys. 226 (2007) 2078–2095.
[17] J.W. Cahn, J.E. Hilliard, Free energy of a nonuniform system. I. Interfacial free energy, J. Chem. Phys. 28 (1958) 258–267.
[18] S.M. Allen, J.W. Cahn, Mechanisms of phase transformations within the miscibility gap of Fe-Rich Fe-Al alloys, Acta Metall. 24 (1976) 425–437.
[19] D. Furihata, A stable and conservative finite difference scheme for the Cahn–Hilliard equation, Numer. Math. 87 (2001) 675–699.
[20] W.J. Boettinger, J.A. Warren, C. Beckermann, A. Karma, Phase-field simulation of solidification, Ann. Rev. Mater. Res. 32 (2002) 163–194.
[21] R. Folch, J. Casademunt, A. Hernandez-Machado, Phase-field model for Hele-Shaw flows with arbitrary viscosity contrast I. Theoretical approach, Phys. Rev. E. 60 (1999) 1724–1733.
[22] P.H. Chiu, Tony W.H. Sheu, On the development of a dispersion-relation-preserving dual-compact upwind scheme for convection-diffusion equation, J. Comput. Phys. 228 (2009) 3640–3655.
[23] Peter C. Chu, Chenwu Fan, A three-point combined compact difference scheme, J. Comput. Phys. 140 (1998) 370–399.
[24] J.U. Brackbill, D.B. Kothe, C. Zemach, A continuum method for modeling surface tension, J. Comput. Phys. 100 (1992) 335–354.
[25] M.W. Williams, D.B. Kothe, E.G. Puckett, Accuracy and convergence of continuum surface-tension models, in: W. Shyy, R. Narayanan (Eds.), Fluid Dynamics at Interfaces, Cambridge University Press, Cambridge, 1998, pp. 294–305.
[26] G.H. Golub, L.C. Huang, H. Simon, W.P. Tang, A fast Poisson solver for the finite difference solution of the incompressible Navier–Stokes equation, SIAM J. Sci. Comput. 19 (1998) 1606–1624.
[27] Christorher K.W. Tam, Jay C. Webb, Dispersion-relation-preserving finite difference schemes for computational acoustics, J. Comput. Phys. 107 (1993) 262–281.
[28] P.H. Chiu, Tony W.H. Sheu, R.K. Lin, Development of a dispersion-relation-preserving upwinding scheme for incompressible Navier–Stokes equations on non-staggered grids, Numer. Heat Transfer B Fundam. 48 (2005) 543–569.
[29] J. Leray, Essai sur le mouvement dun fluid visqueux emplissant lspace, Acat Math. 63 (1934) 193–258.
[30] W.J. Rider, D.B. Kothey, Reconstructing volume tracking, J. Comput. Phys. 141 (1998) 112–152.
[31] S.T. Zalesak, Fully multi-dimensional flux corrected transport algorithm for fluid flow, J. Comput. Phys. 31 (1979) 335–362.
[32] J.C. Martin, W.J. Moyce, An experimental study of the collapse of fluid columns on a rigid horizontal plane, Philos. Trans. Roy. Soc. Lond.: Ser. A 244 (1952) 312–324.
[33] J.L. Guermond, L. Quartapelle, A projection FEM for variable density incompressible flows, J. Comput. Phys. 165 (2000) 167–188.
[34] G. Brereton, D. Korotney, Coaxial and oblique coalescence of two rising bubbles, in: I. Sahin, G. Tryggvason (Eds.), Dynamics of Bubbles and Vortices Near a Free Surface, AMD-Vol. 119, ASME, New York, 1991.
[35] F.H. Harlow, J.P. Shannon, The splash of a liquid drop, J. Appl. Phys. 38 (1967) 3855–3866.
[36] M. Rieber, A. Frohn, A numerical study on the mechanism of splashing, Int. J. Heat Fluid Flow 20 (1999) 453–461.
[37] F. Xiao, A. Ikebata, T. Hasegawa, Numerical simulations of free-interface fluids by a multi integrated moment method, Comput. Struct. 83 (2005) 409–423.
[38] Kensuke Yokoi, A numerical method for free-surface flows and its application to droplet impact on a thin liquid layer, J. Sci. Comput. 35 (2008) 372–396.